High Responsivity, Large-Area Graphene/MoS_2 Flexible Photodetectors

Domenico De Fazio,[†,¶] Ilya Goykhman,[†,¶] Duhee Yoon,[†] Matteo Bruna,[†] Anna Eiden,[†] Silvia Milana,[†] Ugo Sassi,[†] Matteo Barbone,[†] Dumitru Dumcenco,[‡] Kolyo Marinov,[‡] Andras Kis,[‡] and Andrea C. Ferrari[*,†]

Cambridge Graphene Centre, University of Cambridge, Cambridge CB3 0FA, UK, and Electrical Engineering Institute, Ecole Polytechnique Federale de Lausanne, Switzerland

E-mail: acf26@eng.cam.ac.uk

Abstract

We present flexible photodetectors (PDs) for visible wavelengths fabricated by stacking centimetre-scale chemical vapor deposited (CVD) single layer graphene (SLG) and single layer CVD MoS_2, both wet transferred onto a flexible polyethylene terephthalate substrate. The operation mechanism relies on injection of photoexcited electrons from MoS_2 to the SLG channel. The external responsivity is 45.5A/W and the internal 570A/W at 642nm. This is at least two orders of magnitude higher than bulk-semiconductor flexible membranes. The photoconductive gain is up to 4×10^5. The photocurrent is in the 0.1-100μA range. The devices are semi-transparent, with just 8% absorption at 642nm and work stably upon bending to a curvature of 1.4cm. These capabilities and the low voltage operation ($<$1V) make them attractive for wearable applications.

[*]To whom correspondence should be addressed
[†]Cambridge Graphene Centre, University of Cambridge, Cambridge CB3 0FA, UK
[‡]Electrical Engineering Institute, Ecole Polytechnique Federale de Lausanne, Switzerland
[¶]Equal contribution

Modern electronic and opto-electronic systems such as smart phones, smart glasses, smart watches, wearable devices and electronic tattoos increasingly require ultra-thin, transparent, low-cost and energy efficient devices on flexible substrates.[1] The rising demand for flexible electronics and optoelectronics requires materials which can provide a variety of electrical and optical functionalities, with constant performance upon application of strain.[2] A wide range of optoelectronic devices on flexible substrates have been reported to date, such as photodetectors (PDs),[3,4] light emitting diodes (LEDs),[5] optical filters,[6] optical interconnects,[7,8] photovoltaic devices[9,10] and biomedical sensors.[11,12]

Major challenges in the development of flexible optoelectronic devices stem from the limitations associated with the high stiffness of bulk semiconductors.[13,14] In the case of flexible PDs, the current approaches primarily rely on thin (μm-thick) semiconductor membranes[4,15] and compound semiconductor nanowires (NWs),[3,16–18] mainly because of their ability to absorb light throughout the whole visible range (0.4-0.7μm) and the possibility to adapt their fabrication techniques from rigid to plastic, or deformable substrates.[1]

One of the key parameters for PDs characterization is the responsivity. This is defined as the ratio between the collected photocurrent (I_{ph}) and the optical power. The responsivity is named external ($R_{ext} = I_{ph}/P_o$)[19] or internal ($R_{int} = I_{ph}/P_{abs}$),[19] whenever the incident (P_o) or absorbed (P_{abs}) optical power is used at the denominator. Since not all incident photons are absorbed by a PD, i.e. $P_{abs} < P_{in}$, then R_{int} is typically larger than R_{ext}.[19]

In flexible PDs, R_{ext} up to$\sim 0.3A/W$ was reported for crystalline semiconductor membranes (InP, Ge)[4,15] with integrated p-i-n junctions, showing photocurrent up to$\sim 100\mu A$, with$\sim 30\%$ degradation upon bending at a radius $r_b \sim$3cm.[15] PDs made of a single semiconductor NW on flexible substrates[3,16–18] demonstrated R_{ext} up to$\sim 10^5 A/W$, for r_b down to 0.3cm.[3] Yet, these provide limited I_{ph} in the order of nA[3,16,18] up to less than $1\mu A$.[17] For flexible devices exploiting NW-arrays by drop-casting,[3,16,18] rather than based on single-NWs, R_{ext} degrades significantly from$\sim 10^5 A/W$ to the mA/W range,[3,16,18] due to photocurrent loss at multiple junctions in the NW network.[3,16,18]

Graphene and related materials (GRMs) have great potential in photonics and optoelectronics.[20–23] A variety of GRM-based devices have been reported, such as flexible displays,[24] photovoltaic modules,[25,26] photodetectors,[22,27–29] optical modulators,[30] plasmonic devices,[31–35] and ultra-fast lasers.[23] Heterostructures, obtained by stacking layers of different materials were also explored,[21,22] e.g. in photovoltaic[36] and light emitting devices.[37]

Flexible PDs based on graphene and related materials (GRM) were studied for ultraviolet,[38,39] visible[40–45] and near infrared bands.[46,47] In these devices, different materials and heterostructures produced by mechanical exfoliation,[40,41] CVD,[42,43,46] and liquid phase exfoliation (LPE)[44,45,47] were employed. The flexible PDs produced by mechanical exfoliation[40,41] have a small (μm^2) photoactive area, and they cannot be scaled up to mass production. LPE-based PDs have low ($<$mA/W)[44,45] responsivity. Ref. 47 showed that thick (μm) films of chemically modified and charge-transfer optimized LPE/polymer composites can provide$\sim$A/W responsivity[47] at near infrared bands. Nevertheless, these PDs require high (10V) operation voltage and are non-transparent. Flexible PDs at 450nm using CVD MoS_2 transistors[42] and MoS_2/WS_2 heterostructures[43] were previously reported, and PDs at 780nm were prepared from doped SLG pn-junctions.[38] However, these devices have responsivity in the mA/W range. CVD-based SLG/MoS_2 heterostructures[48] showed good photodetection on rigid Si/SiO_2 substrates, with back-gate dependent $R_{int} \sim 10^8$A/W for optical intensities <0.1pW/μm^2.

Here we demonstrate a polymer electrolyte gated, CVD-based flexible PD for visible wavelengths with large (mm^2) photoactive area combined with high responsivity (hundreds A/W), high ($>80\%$) transparency, gate tunability, low ($<$1V) operation voltage and stable ($\pm 12\%$) I_{ph} upon multiple (>30) bending cycles with bending radius $<$1.4cm. The device is assembled by stacking on a PET substrate a centimetre-scale CVD SLG on top of a CVD-grown single layer MoS_2 (1L-MoS_2). In this configuration, 1L-MoS_2 acts as visible light absorber, while SLG is the conductive channel for photocurrent flow.[48] We show that R_{ext} increases either by promoting the carrier injection from 1L-MoS_2 to SLG using polymer electrolyte gating, or by increasing the source-drain voltage. This R_{ext} is achieved in devices with$\sim 82\%$ transparency, twice that reported for

semiconductor membrane devices.[15] We get $R_{int} \sim 570$A/W for$\sim$0.1nW/μm^2 at 642nm, similar to SLG/MoS_2 PDs[48] on rigid substrate operating at the same optical power level. This shows that SLG/MoS_2 heterostructures on PET retain their photodetection capabilities. Upon bending, our devices have stable performance for r_b down to$\sim$ 1.4cm. This is comparable to r_b measured in semiconductor membranes PDs,[4,15] which show lower ($< 0.3A/W$) responsivities.[4,15] Although our r_b is one order of magnitude larger than for flexible single NWs,[3,16–18] the latter had at least three orders of magnitude smaller device areas ($< 5\mu m^2$)[3,16–18] compared to our PDs ($> 0.2mm^2$). Given the responsivity, flexibility, transparency and low operation voltage (below $1V$), our PDs may be integrated in wearable, biomedical and low-power opto-electronic applications.[11,12,17]

Results and discussion

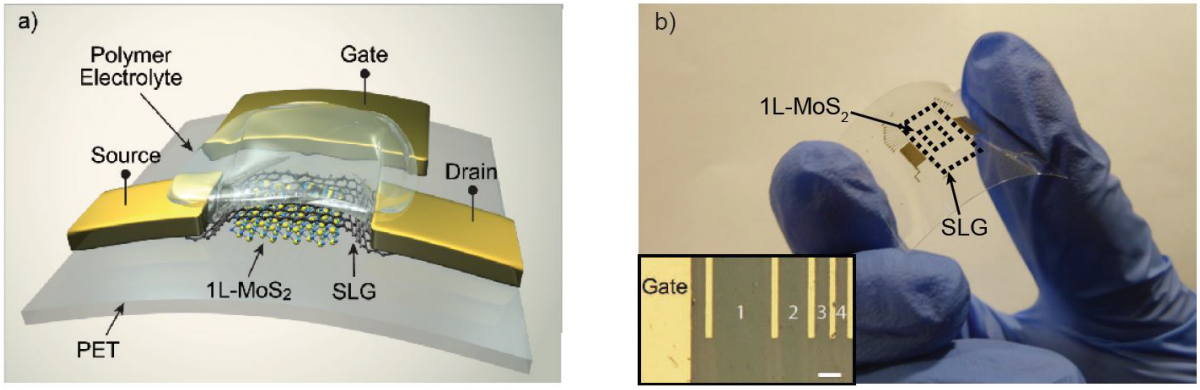

Figure 1: a) Schematic SLG/MoS_2 flexible PD, side-gated with a polymer electrolyte. b) Picture of a typical PD, showing transparency and flexibility. (Inset) Optical image of 4 PDs with different channel lengths and common side gate electrode. Scale bar is 200μm.

Fig.1 plots a schematic drawing of our PDs. We fabricated 4 PD arrays with 10 devices each, with channel lengths of 100μm, 200μm, 500μm and 1mm. Each device consists of a 1L-MoS_2 absorber covered by a SLG channel, clamped between source and drain electrodes. We chose PET as a flexible substrate due to its$\sim$90% transparency in the visible range[49] and ability to withstand solvents (e.g acetone and isopropyl alcohol)[50] commonly used in the transfer processes of layered materials grown by CVD (e.g. transfer of SLG grown on Cu[51]). A 1L-MoS_2 is used as

absorber in order to preserve a >80% transparency, considered suitable by industry for wearable applications.[52] The SLG/1L-MoS_2 heterostructure is gated using a polymer electrolyte.[53,54]

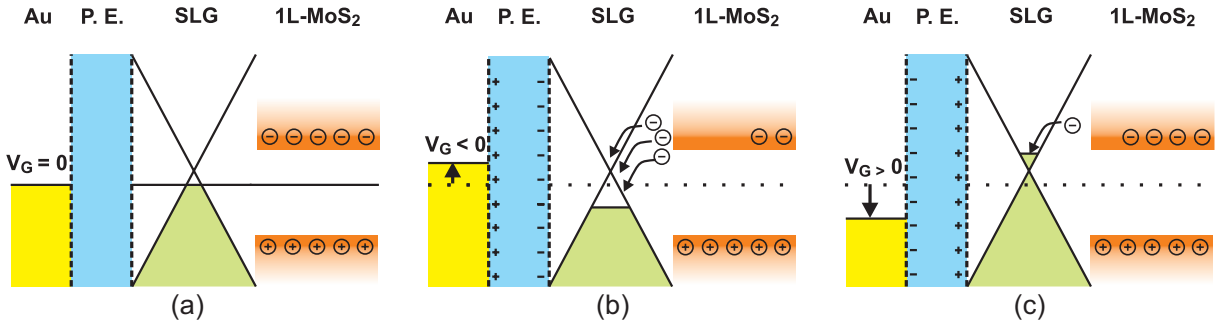

Figure 2: Schematic band diagram of polymer electrolyte (PE) gated SLG/1L-MoS_2 PD at a) zero, b) negative and c) positive V_{GS}

The operation principle of our devices is depicted in Fig.2. For energy bands alignment, the electron affinity of 1L-MoS_2 and the Dirac point of SLG are assumed to be$\sim$4-4.2eV[55,56] and$\sim$4.6eV,[57,58] respectively. We also assume SLG to be initially p-doped (Fig.2a), as reported in previous works involving SLG transferred on PET.[59,60] At zero voltage the device is in thermodynamic equilibrium with a constant Fermi level (E_F) across the structure and zero current flow between the layers. SLG is initially p-doped (Fig.2a), so that E_F is initially located below the Dirac point. During illumination and photon absorption in MoS_2, part of the photo-generated electrons would be injected from the 1L-MoS_2 conduction band into the lower energy states in p-doped SLG,[48] leaving behind the uncompensated charge of photogenerated holes. The latter would be trapped in 1L-MoS_2 and act as an additional positive V_{GS} to the SLG channel, seen as a shift of the charge neutrality point (V_{CNP}) to more negative voltages. In p-doped SLG, the injected electrons from 1L-MoS_2 would occupy energy states above E_F (Fig.2b), thus reducing the holes concentration and decreasing the holes current in the SLG channel. Electron injection can be further promoted by gating. When negative V_{GS} is applied, higher p-doping of the SLG channel would induce a stronger electric field at the SLG/1L-MoS_2 interface,[48] thus favoring electron transfer from 1L-MoS_2 (Fig.2b). Hence, for negative V_{GS}, R_{ext} is expected to increase, due to injection of more photo-electrons to SLG and consequent more pronounced PD current reduction. The opposite should happen for positive V_{GS}, where the gate-induced negative charge in SLG

would reduce the p-doping and shift E_F towards the Dirac point. In this case, the photogenerated electrons in 1L-MoS_2 would experience weaker electric fields at the SLG/1L-MoS_2 interface,[48] and would become less attracted by the SLG channel. Thus, we expect R_{ext} to decrease. For high enough positive V_{GS}, E_F crosses the Dirac point, and SLG becomes n-doped (Fig.2c). As a result, only a weak electron injection from 1L-MoS_2 would be possible, if E_F in SLG remains below the 1L-MoS_2 conduction band, retaining a weak electric field at the interface. In this regime, the transferred electrons increase the free carrier concentration in the n-doped channel, hence only minor increments of R_{ext} and I_{ph} are expected.

Our devices are built as follows. 1L-MoS_2 is epitaxially grown by CVD on c-plane sapphire substrates.[61] These are annealed at 1000°C in air for 1 hour after consecutive cleaning by acetone/isopropyl alcohol/deionized (DI) water. They are then placed face-down above a crucible containing$\sim$5mg MoO_3 ($\geq$99.998% Alfa Aesar). This is loaded into a 32mm outer diameter quartz tube placed in a split-tube three-zone furnace. A second crucible containing 350mg sulfur ($\geq$ 99.99% purity, Sigma Aldrich) is located upstream from the growth substrates. Ultrahigh-purity Ar is used as carrier gas at atmospheric pressure. The procedure is: ramp the temperature to 300°C with 200sccm Ar flow, set to 300°C for 10mins, ramp to 700°C (50°C/min increase temperature rate) with 10sccm Ar flow, set at 700°C for 10 min, cool to 570°C with 10sccm of Ar, increase the gas flow to 200sccm and open the furnace for rapid cooling.[61] SLG is grown on a 35μm Cu foil, following the process described in Ref. 51. The substrate is annealed in hydrogen atmosphere (H_2, 20sccm) up to 1000°C for 30 minutes. Then, 5sccm CH_4 is added to initiate growth.[51,62] The sample is then cooled in vacuum (1mTorr) to room temperature and removed from the chamber.

Prior to assembling the SLG/MoS_2 stack, the quality and uniformity of MoS_2 on sapphire and SLG on Cu are inspected by Raman spectroscopy and photoluminescence (PL), using a Horiba Jobin Yvon HR800 spectrometer equipped with a 100X objective. The laser power is kept below 100μW (spot size $< 1\mu$m in diameter) to avoid possible heating effects or damage. Fig.3a (green curve) plots the Raman spectrum of CVD MoS_2 on sapphire for 514nm excitation. The peak at$\sim$ 385cm^{-1} corresponds to the in-plane (E^1_{2g}) mode,[63,64] while that at$\sim$404cm^{-1}, is the out of plane

(A_{1g}) mode,[63,64] with full width at half maximum FWHM(E^1_{2g})=2.5 and FWHM(A_{1g})=3.6cm^{-1}, respectively. The E^1_{2g} mode softens, whereas the A_{1g} stiffens with increasing layer thickness,[65,66] so that their frequency difference can be used to monitor the number of layers.[65] The peak position difference$\sim$20cm^{-1} is an indicator of 1L-MoS_2.[65] The peak at$\sim$ 417cm^{-1} (marked by asterisk in Fig.3a) corresponds to the A_{1g} mode of sapphire.[67]

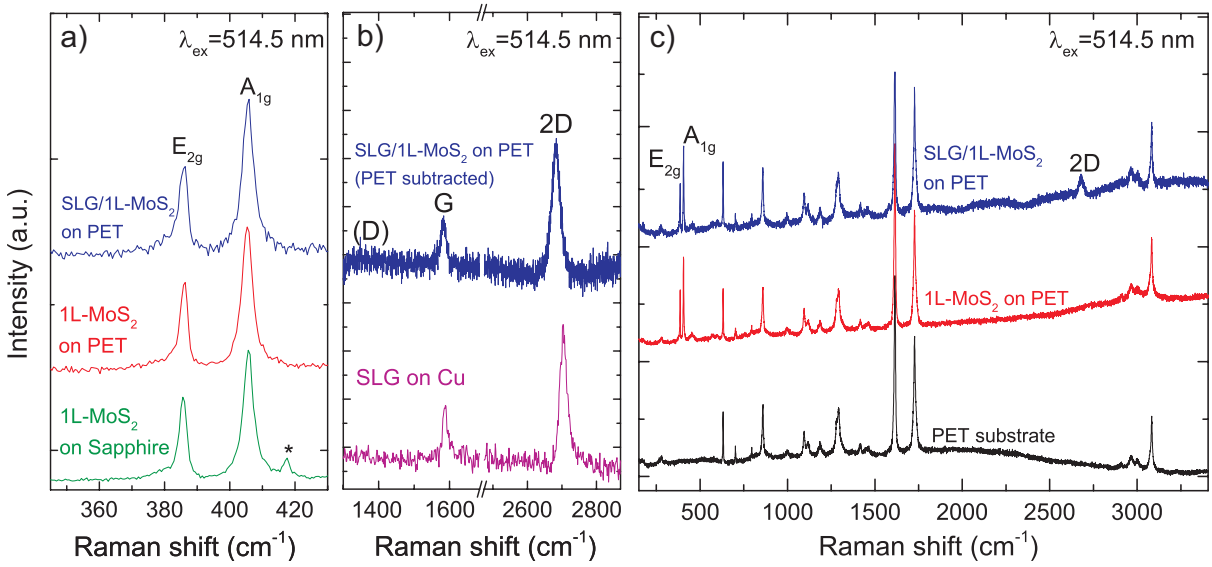

Figure 3: (a) Raman spectra at 514nm for 1L-MoS_2 on sapphire, 1L-MoS_2 on PET, and SLG/1L-MoS_2. (b) Comparison at 514nm of the Raman spectra of as-grown SLG on Cu (magenta curve) with SLG/1L-MoS_2 after transfer on PET. (c) Raman spectra at 514nm of PET substrate (black curve), 1L-MoS_2 on PET (red curve) and SLG/1L-MoS_2 on PET (blue curve).

The Raman spectrum measured at 514 nm of SLG on Cu is shown in Fig.3b (magenta curve). This is obtained after the removal of the non-flat background PL of Cu.[68] The two most intense features are the G and the 2D peak, with no significant D peak. The G peak corresponds to the E_{2g} phonon at the Brillouin zone centre.[69] The D peak is due to the breathing modes of sp^2 rings and requires a defect for its activation by double resonance.[69–72] The 2D peak is the second order of the D peak.[69] This is always seen, even when no D peak is present, since no defects are required for the activation of two phonons with the same momentum, one backscattering from the other.[69] In our sample, the 2D peak is a single sharp Lorentzian with FWHM(2D)$\sim$26cm^{-1}, a signature of SLG.[70] Different ($\sim$20) measurements show similar spectra, indicating uniform quality throughout the sample. The position of the G peak, Pos(G), is$\sim$1588cm^{-1}, with FWHM(G)$\sim$16cm^{-1}. The

2D peak position, Pos(2D) is$\sim$2705cm^{-1}, while the 2D to G peak area ratio , indicating a p-doping$\sim$300meV,[53,73,74] which corresponds to a carrier concentration $\sim 6\cdot 10^{12}$cm^{-2}.

Another evidence for 1L-MoS_2 comes from the PL spectrum [Fig.4a (green curve)], showing a peak$\sim$658nm ($\sim$1.88eV), due to band-to-band radiative recombination in 1L-MoS_2.[75]

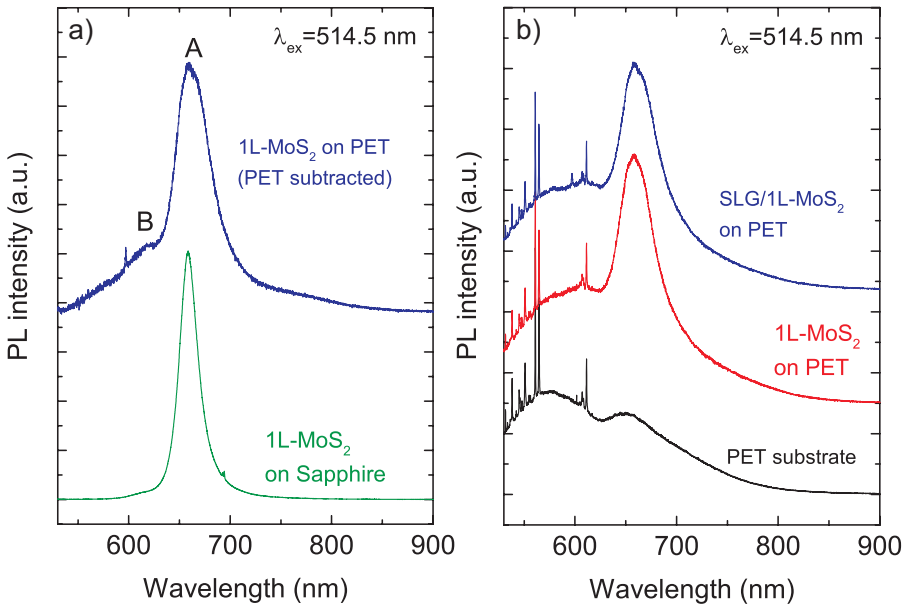

Figure 4: (a) PL spectrum at 514nm (2.41eV) of 1L-MoS_2 on sapphire, and SLG/1L-MoS_2 after transfer on PET. (b) PL spectra of PET substrate (black curve), 1L-MoS_2 on PET (red curve) and SLG/1L-MoS_2 on PET (blue curve).

Then, the MoS_2 film is transferred onto a PET substrate from sapphire using a KOH-based approach.[61] The samples are first spin coated with$\sim$100nm polymethyl methacrylate (PMMA). This is detached in a 30% KOH solution, washed in DI water and transferred onto PET. The PMMA is then dissolved in acetone. Subsequently, SLG is transferred on the 1L-MoS_2 on PET. PMMA is spin coated on the SLG/Cu substrate, then placed in a solution of ammonium persulfate (APS) in DI water until Cu is etched.[51,76] The PMMA membrane with attached SLG is then transferred to a beaker filled with DI water for cleaning APS residuals. The membrane is subsequently lifted with the target PET substrate having 1L-MoS_2 on top. After drying, PMMA is removed in acetone leaving SLG on 1L-MoS_2.

Raman and PL characterizations are performed at each step of the SLG/1L-MoS_2 assembly

on PET, i.e on 1L-MoS_2 transferred on PET, and on SLG on 1L-MoS_2. This is to confirm no degradation during the fabrication process. For 1L-MoS_2 on PET, the Raman at 514nm is shown, with a close-up of the E^1_{2g} and A_{1g} regions, in Fig.3a (red curve). The frequency difference between E^1_{2g} and A_{1g} and the FWHMs are preserved on PET, suggesting no degradation. The PL spectrum of 1L-MoS_2 on PET is shown in Fig.4b (red curve). The signal from 1L-MoS_2 is convolved within the background due to the PET substrate [Fig.4b (black curve)]. In order to reveal the underlying PL signature of 1L-MoS_2, we use a point-to-point subtraction between the spectrum of 1L-MoS_2 on PET [Fig.4b (red curve)] and the reference PET spectrum [Fig.4b (black curve)]. Prior to subtraction, the spectra are normalized to the intensity of the Raman peak at$\sim$1615cm^{-1} (corresponding to the peak at$\sim$560nm in Fig.4b), due to the stretching vibrations of benzene rings in PET.[77] As a result, the PL signal of 1L-MoS_2 can be seen in Fig.4a (blue curve) revealing no significant changes after transfer. The subsequent transfer of SLG on 1L-MoS_2 does not alter the 1L-MoS_2 PL position and lineshape [Fig.4b (blue curve)].

We then characterize the SLG transferred on 1L-MoS_2/PET. The intense Raman features of the underlying PET substrate[77] [Fig.3c (black curve)], mask the SLG peaks. In order to reveal the Raman signatures of SLG, we first measure the reference spectrum, shown in Fig.3c (black curve), of a PET substrate, using identical experimental conditions as those for SLG/1L-MoS_2/PET. We then implement a point-to-point subtraction, normalized to the intensity of the PET peak at$\sim$1615cm^{-1}, of the PET reference spectrum from the total spectrum Fig.3c (blue curve). The result is in Fig.3b (blue curve). The 2D peak retains its single-Lorentzian line-shape with FWHM(2D)$\sim$28cm^{-1}, validating the transfer of SLG. The negligible D peak indicates that no significant defects are induced during transfer. Pos(G) is$\sim$1583cm^{-1}, FWHM(G)$\sim$17cm^{-1}, Pos(2D)$\sim$2683cm^{-1} and A(2D)/A(G)$\sim$4.8, indicating a p-doping$\sim 4\cdot 10^{12}$cm^{-2} ($\sim$250meV).[53,73]

We then measure the absorption and transmission of SLG/1L-MoS_2 using a broadband (400-1300nm) white light from a tungsten halogen lamp. The transmitted light is collected by a 10x objective lens (NA=0.25) with a Horiba Jobin Yvon HR800 spectrometer equipped with a 300 grooves/mm grating, charged coupled device (CCD) detector and a 50μm pinhole. Fig.5a plots

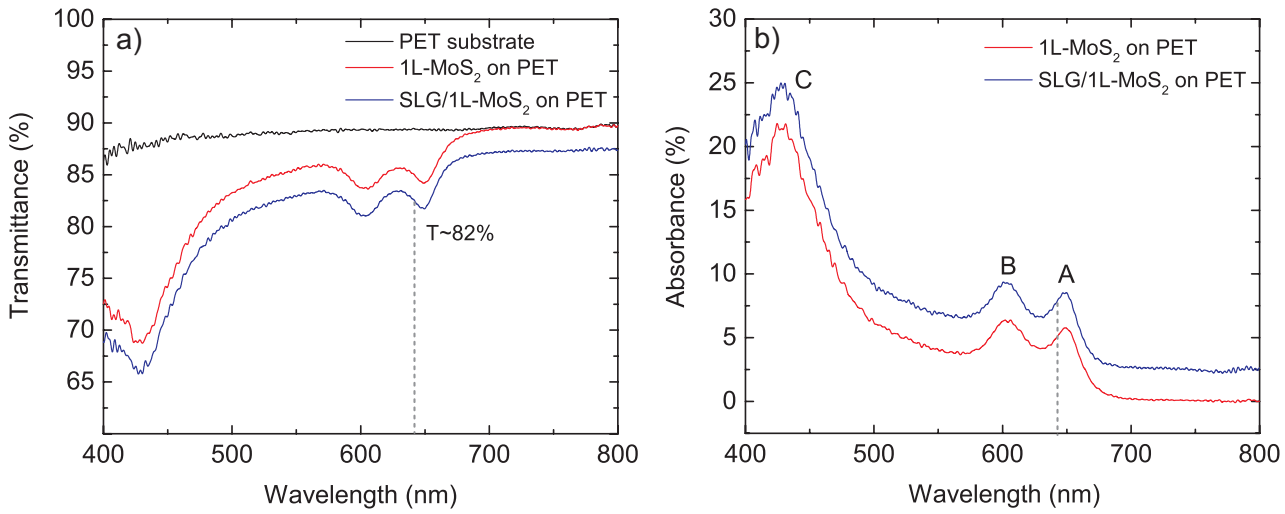

Figure 5: (a) Transmittance of PET (black curve), 1L-MoS_2 on PET (red curve) and SLG/1L-MoS_2 on PET (blue curve). (b) Absorbance of 1L-MoS_2 and SLG/1L-MoS_2 as derived from the transmittance measurements. Dashed lines indicate our test wavelength.

the optical transmittance of bare PET (T_{PET}, black line), 1L-MoS_2 on PET (T_{MoS_2}, red line) and the final SLG/1L-MoS_2 stack on PET (T_{Hetero}, blue line) measured in the 400-800nm wavelength range. Fig.5b plots the absorption of 1L-MoS_2 on PET (Abs_{MoS_2}, red line) and of SLG/1L-MoS_2 on PET (Abs_{Hetero}, blue line), calculated as Abs_{MoS_2}=(T_{PET}-T_{MoS_2})/T_{PET} and Abs_{Hetero}=(T_{PET}-T_{Hetero})/T_{PET}. The three peaks in Fig.5b at ∼650nm (1.91eV), ∼603nm (2.06eV), and ∼428nm (2.90eV) correspond to the A, B, C excitons of 1L-MoS_2.[75,78] The positions of the A, B and C peaks remain unchanged after SLG transfer. The *Abs* difference between the two curves (red and blue) is∼2.6%, consistent with the additional SLG absorption.[79]

The PD area is shaped by etching, whereby SLG extending beyond the 1L-MoS_2 layer is removed in an oxygen plasma. The source-drain and gate electrodes are then defined by patterning the contacts area, followed by Cr/Au (6nm/60nm) evaporation and lift-off. PDs with different channels lengths (100μm-1mm), 2mm channel width and common side-gate electrodes (1cm x 0.5cm) are built, Fig.1b.

Ref. 48 showed that the responsivity of SLG/MoS_2 PDs can be enhanced by gating. This induces a stronger electric field at the SLG/MoS_2 interface and promotes charge transfer. Various gating techniques have been exploited for GRM-based devices, including conventional Si/SiO_2

back-gates,[80] high-k dielectrics (Al_2O_3, HfO_2),[81] chemical dopants,[82] ionic liquids[83] and polymer electrolytes (PE).[53,74] In order to gate our SLG/1L-MoS_2 on PET, we employ the latter due to its compatibility with flexible substrates[84] and the ability to substantially dope SLG ($\pm 0.8eV$)[53,74] using small gate voltages (up to 4V), unlike other gating techniques, which would require considerably higher biases to reach the same doping.[80,82] We use a PE consisting of $LiClO_4$ and polyethylene oxide (POE).[53,74] We place the PE over both the SLG channel and the side-gate electrode. To evaluate the effect of PE deposition on the SLG channel doping we use Raman analysis (Pos(G)$\sim$1583cm^{-1}, FWHM(G)$\sim$19cm^{-1}, Pos(2D)$\sim$2686cm^{-1} and A(2D)/A(G)$\sim$5.3, p-doping $\sim$230meV)[53,73]) and find a small reduction of p-doping. For electrical measurements we apply $-1V < V_{GS} < 1V$ in order to avoid electrochemical reactions, such as hydrolysis of residual water in the electrolyte.[85,86] These reactions may permanently modify the graphene electrode,[85,86] and compromise the stability and performance of the device. To control the stability of the PE gating we continuously monitor the gate leakage current (I_{gate}) and obtain $I_{gate} < 1$nA throughout the experiments. The devices were tested$\sim$30 times, showing no degradation in the leakage current over at least six months.

We characterize the responsivity at 642nm ($\sim$1.93eV), slightly above the A exciton peak, where absorption of 1L-MoS_2 is maximized (Fig.5b). At 642nm the SLG/1L-MoS_2 heterostructure shows$\sim$8% absorption (Fig.5b) and the device retains$\sim$82% transparency (Fig.5a).

The $I_{DS}-V_{GS}$ measurements in Fig.6a are done at room temperature using a probe station and a parameter analyzer (Keithley 4200). The PD is illuminated at normal incidence by a collimated laser with P_o ranging from 100μW to 4mW. At these P_o and with $V_{DS} = 0.1V$ we measure a positive V_{CNP} ranging from$\sim 0.39V$ to $0.47V$, indicating an initial SLG p-doping$\sim$220meV, consistent with the Raman estimate.

Fig.6a shows that, for $-1V < V_{GS} < 0.5V$ where SLG transport is hole dominated, the current decreases under illumination ($\sim 10\mu A$ at $V_{GS} = -1V$), as anticipated from the band-diagram of Fig.2. For $V_{GS} > 0.5V$, where SLG is electron-doped, the PD shows a small (up to$\sim 0.2\mu A$) current increase under illumination. Fig.6b plots R_{ext} as a function of V_{GS}, as derived from transcon-

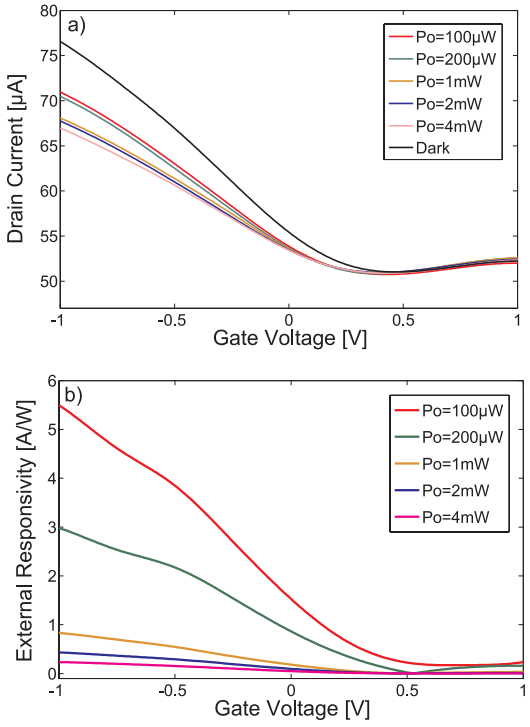

Figure 6: a) Transfer characteristics as a function of P_o. b) R_{ext} as a function of V_{GS} and P_o. Channel length and width are 100μm and 2mm respectively.

ductance measurements using:[19]

$$R_{ext} = \frac{|\, I_{light} - I_{dark} \,|}{P_o \cdot A_{PD}/A_o} \tag{1}$$

where I_{light} and I_{dark} are the PD current under illumination and in dark, $|\, I_{light} - I_{dark} \,| = I_{ph}$ is the photocurrent defined as the absolute change in the device current upon illumination, A_o is the laser spot area, A_{PD} is the PD area, and A_{PD}/A_o is a scaling factor that takes into account the fact that only a fraction of optical power impinges on the PD. As expected from the band-diagram in Fig.2, R_{ext} tends to increase for more negative V_{GS}, up to$\sim 5.5A/W$ at $V_{GS} = -1V$, $V_{DS} = 0.1V$ for $P_o = 100\mu W$. By taking into account that only 8% of light is absorbed ($P_{abs} = 0.08 \cdot P_o$), we derive $R_{int} = R_{ext}/0.08 = 69A/W$. Fig.6b implies that the higher P_o, the lower R_{ext}. This can be explained considering that the more photo-generated electrons are injected into the p-doped channel, the lower the electric field at the SLG/1L-MoS_2 interface, therefore a reduced injection of electrons causes R_{ext} to decrease.

Given that $R_{ext}, R_{int} > 1A/W$, we expect a photoconductive gain (G_{PD}),[19,87] whereby absorp-

tion of one photon results in multiple charge carriers contributing to I_{ph}. Our PDs act as optically-gated photoconductors, where the SLG conductance is modulated by optical absorption in the 1L-MoS_2. In this configuration, the presence of G_{PD} implies that the injected electrons in SLG can recirculate multiple times between source and drain, before recombining with trapped holes in 1L-MoS_2. Consequently, G_{PD} can be estimated as the ratio of electrons recombination (τ_{rec}) and transit (t_{tr}) times in the SLG channel: $G_{PD} = \tau_{rec}/t_{tr}$.[19,21,22,87] For higher V_{DS}, the free carriers drift velocity υ_d in the SLG channel increases linearly with bias (Ohmic region) until it saturates, because of carriers scattering with optical phonons.[88] The linear increase in υ_d results in shorter t_{tr}, with $t_{tr} = L/\upsilon_d$, where L is the channel length.[19,21,22,87] Therefore, G_{PD} is also expected to grow linearly with V_{DS}, providing higher R_{ext}. To confirm the photoconductive nature of G_{PD} in our devices and test the dependence of R_{ext} on V_{DS}, we measure $I_{DS} - V_{DS}$ under illumination at $P_o = 100\mu W$ for $V_{GS} = -1V$ and calculate R_{ext} using Eq.1. The $I_{DS} - V_{DS}$ characteristics of the PD show linear dependence, confirming Ohmic behavior of the metal-SLG-metal channel.[89] We use $V_{DS} < 1V$ to keep the device operation in the linear (Ohmic) regime and minimize the effects of the non-linear dependence of υ_d on V_{DS} (such as velocity saturation) that might appear for $V_{DS} > 1V$.[88] As shown in Fig.7, R_{ext} scales with V_{DS} and reaches$\sim 45.5A/W$ ($R_{int} \sim 570A/W$) at $V_{DS} = 1V$. This is almost one order of magnitude higher than at $V_{DS} = 0.1V$, consistent with the similar increase in V_{DS}. These results are at least two orders of magnitude higher than semiconductor flexible membranes.[4,15] Furthermore, such combination of high (hundreds A/W) responsivity with μA range photocurrent overcome that found in other GRM-based PDs in the visible range.[40–45,47] We also fabricate a control device with a 1L-MoS_2 channel only, without SLG. This device has $R_{ext} \sim 2mA/W$, which is four orders of magnitude smaller than that of our SLG/1L-MoS_2 heterostructure. We thus conclude that SLG/1L-MoS_2 heterostructures are necessary to achieve high (hundreds A/W) responsivity, due to the presence of photoconductive gain.

To assess the photoresponse uniformity in our SLG/1L-MoS_2 heterostructures, we perform photocurrent mapping using the same laser source (642nm) as for opto-electronic characterizations. We scan areas of $80\mu m \times 140\mu m$ (pixel size $3\mu m \times 3\mu m$) at different locations. At each

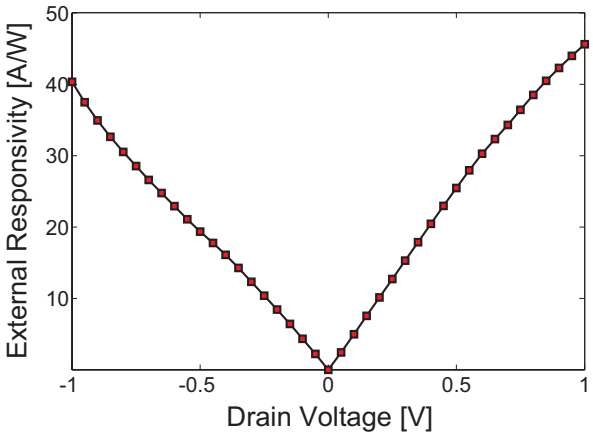

Figure 7: R_{ext} as a function of V_{DS} for $P_o = 100\mu W$ at $V_{GS} = -1V$.

position (pixel) the device photocurrent is measured (Fig.8a), while V_{DS}=0.3V is applied. We also collect the backscattered light to give a reflection map (Fig.8b). Fig.8a indicates that the entire channel area confined between the source-drain electrodes is photoactive and shows uniform photocurrent photoresponse with standard deviation $\pm 15\%$. We thus conclude that interface imperfections (e.g. bubbles, polymer residuals etc.) have minor effect on the charge transfer process from MoS_2 to graphene.

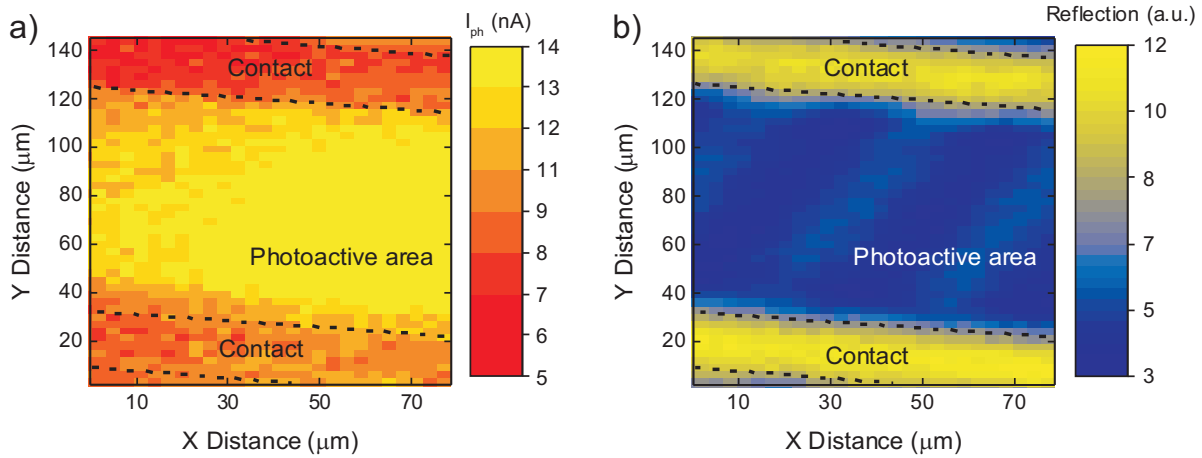

Figure 8: a) Photocurrent map of channel area, simultaneously measured with backscattered light map. A uniform signal is observed in the channel area (between the electrodes). b) Reflection map of backscattered light from the device channel. The yellow areas, corresponding to the contact areas, show higher reflectance than the substrate (in blue).

We define G_{PD} as the ratio between electrons recirculating in the SLG channel, thus sustaining

I_{ph}, and the initial electron concentration injected into SLG from 1L-MoS_2:[48]

$$G_{PD} = \frac{|\, I_{light} - I_{dark} \,|}{q \cdot A_{PD} \cdot \Delta n_{ch}} \tag{2}$$

where q is the electron charge and Δn_{ch} is the concentration per unit area of the injected electrons. Δn_{ch} is equal to the trapped-hole concentration in 1L-MoS_2, which is related to a charge neutrality point shift $\Delta V_{GS} = \Delta V_{CNP}$ in the transfer characteristics. To calculate Δn_{ch}, we first write the potential balance in the metal-dielectric-SLG structure. When V_G is applied, it creates a gate-to-channel potential drop (V_{diel}), and it induces a local electrostatic potential in the graphene channel ($V_{ch} = E_F/q$):[19,53]

$$V_G = V_{diel} + V_{ch} = \frac{Q_G}{C_G} + V_{ch} \tag{3}$$

where Q_G and C_G are the charge concentration and the geometrical capacitance per unit area associated with the gate electrode respectively. $|Q_G| = |q \cdot n_{ch}|$, reflecting the charge neutrality of the gate capacitor, with n_{ch} the charge carrier concentration per unit area in the channel. Any variations Δn_{ch} change ΔV_G. As a result:

$$\frac{dV_G}{dQ_G} = \frac{1}{C_G} + \frac{dV_{ch}}{dQ_G} \tag{4}$$

which leads to:

$$\Delta Q_G = (1/C_G + 1/C_Q)^{-1} \cdot \Delta V_G \tag{5}$$

where $C_Q = dQ_G/dV_{ch}$ is the SLG quantum capacitance[90,91] that characterizes the changes of the channel potential ΔV_{ch} as a result of additional gating ΔQ_G, and $(1/C_G + 1/C_Q)^{-1}$ is the total capacitance C_{tot}.

To calculate Q_G we first need to find C_G and C_Q. In PE gating, C_G is associated with the EDL at the SLG/electrolyte interface.[53,90,92,93] The EDL acts like a parallel-plate capacitor with a dielectric layer thickness of the order of λ_D, so that $C_G = C_{EDL} = \varepsilon\varepsilon_0/\lambda_D$, where ε is the PE dielectric constant, and ε_0 is the vacuum permittivity. In principle, for a monovalent electrolyte, λ_D can be explicitly calculated[94] if the electrolyte concentration is known. However, in the presence

of a polymer matrix, the electrolyte ions can form complexes with polymer chains,[95] therefore the precise ion concentration is difficult to measure. For PE gating, different EDL thicknesses in the range$\sim 1-5nm$ have been reported.[53,54,92,93] To estimate C_{EDL} in our devices we take $\lambda_D \sim 2nm$[53] and the dielectric constant of the PEO matrix to be $\varepsilon \sim 5$,[96] as done in Ref. 53. As a result, we obtain $C_{EDL} = 2.2 \times 10^{-6} F/cm^2$. This is the same order of magnitude as the SLG C_Q.[90] Therefore the latter cannot be neglected in Eq.5. C_Q is given by:[90]

$$C_Q \approx \frac{2q^2}{\hbar v_F \sqrt{\pi}} \cdot \sqrt{n_{ch} + n_i} \tag{6}$$

where $\hbar$ is the reduced Planck constant, $v_F = 1.1 \cdot 10^6 m/s$ is the Fermi velocity of charge carriers in graphene[80,97] and n_i is the intrinsic carrier concentration in SLG near the Dirac point induced by charge impurities, defects and local potential fluctuations in the SLG channel.[90,98–100] Using Raman and transconductance we estimate $n_i \sim 3 \cdot 10^{12} cm^{-2}$. From Eq.6 we then get $C_Q = 4 \cdot 10^{-6} F/cm^2$ at V_{CNP}. From Fig.6a, and extracting ΔV_{CNP} between the dark current and the transfer curves measured under illumination, and with Eq.5, we get Δn_{ch} ranging from $4 - 8 \cdot 10^{11} cm^{-2}$ for P_o going from $100\mu W$ to $4mW$. As a result, we obtain $G_{PD} \sim 5 \times 10^4$ at $V_{DS} = 0.1V$ for different P_o as shown in Fig.9. As discussed previously, G_{PD} becomes larger for higher V_{DS}. Thus, we measure an increase of almost one order of magnitude ($G_{PD} \sim 4 \cdot 10^5$ at $P_o = 100\mu W$) for V_{DS} going from $0.1V$ to $1V$.

Finally, we test I_{ph} as a function of bending using a Deben Microtest three-point bending setup (Fig.10a). The bending radius r_b is estimated as $r_b = (h^2 + (L/2)^2)/2h$, where L is the chord of circumference connecting the two ends of the arc, and h is the height at the chord midpoint. The plotted values of I_{ph} in the bent state at each r_b ($I_{ph,bend}$) are normalized to the value of I_{ph} measured at rest with the sample in flat position ($I_{ph,rest}$). Fig.10b plots the normalized $I_{ph,bend}/I_{ph,rest}$ for different r_b, showing deviations within 15% for r_b down to $1.4cm$. Our value of r_b is comparable to that reported for semiconductor membrane PDs,[4,15] yet the latter show two orders of magnitude lower ($< 0.3A/W$) responsivities.[4,15] Although our r_b is five times larger than the one reported by

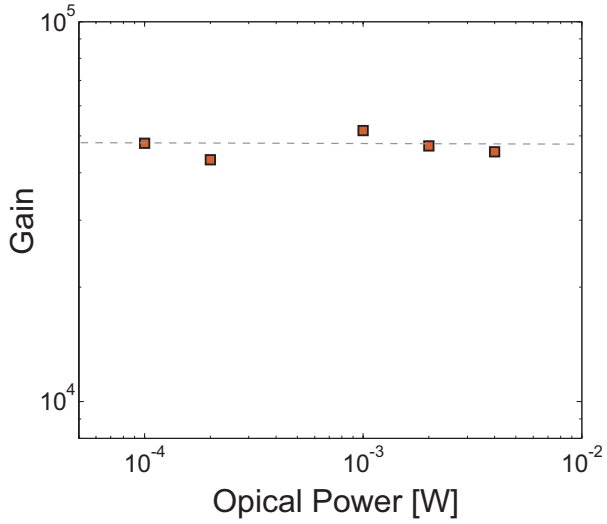

Figure 9: G_{PD} as a function of P_o at $V_{GS} = -1V$ and $V_{DS} = 0.1V$.

flexible single NW devices,[3,16–18] the device area of the tested PD ($> 40mm^2$) is at least six orders of magnitude larger compared to the single NW devices ($< 5\mu m^2$). To test the device performance upon bending cycles, we first re-measure the photocurrent at rest ($I_{ph,rest}$, flat position) and then at the maximal bending (i.e smallest bending radius) allowed by our setup ($I_{ph,bend}$ bending radius 1.4cm), repeating these measurements for 30 bending cycles. Fig.10c plots $I_{ph,bend}/I_{ph,rest}$ as function of bending cycles. This shows that our PDs retain stable photocurrent after multiple bending tests with a $I_{ph,bend}/I_{ph,rest}$ standard deviation $\pm 12\%$.

Conclusions

We reported polymer electrolyte gated flexible photodetectors for visible wavelengths with external responsivity up to$\sim$45.5A/W, photoconductive gain of 4×10^5, operation voltage $<$ 1V and optical transparency$>$ 82%. The responsivity is at least two orders of magnitude higher than in semiconductor flexible membranes. The devices show stable performance upon bending for radii of curvature larger than$\sim$1.4cm. Owing to their responsivity, flexibility, transparency and low operation voltage, our photodetectors can be an attractive candidates to be integrated in wearable, biomedical and low-power opto-electronic applications.[11,12,17]

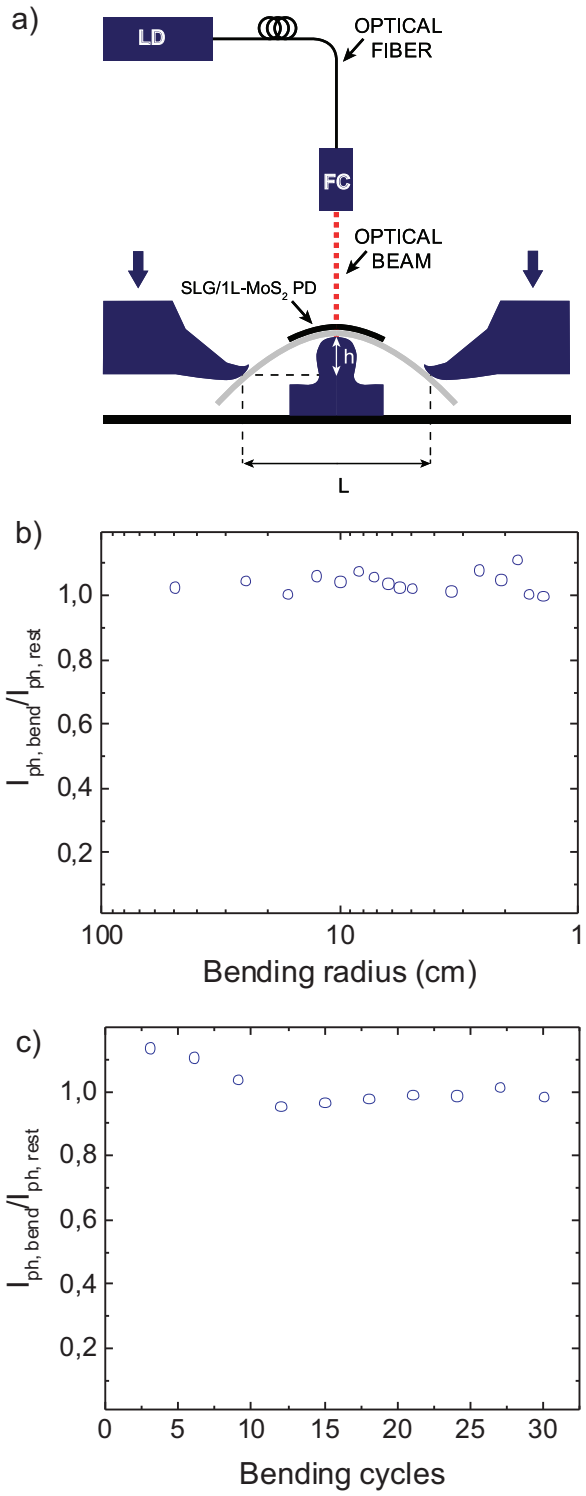

Figure 10: a) Schematic three-point bending setup. LD = laser diode; FC= fiber collimator; b) $I_{ph,bend}$ normalized to the value at rest $I_{ph,rest}$ as a function of r_b; c) $I_{ph,bend}$ normalized to the value at rest $I_{ph,rest}$ upon several bending cycles

Acknowledgement

We acknowledge funding from the EU Graphene Flagship, ERC Grant Hetero2D, and EPSRC Grant Nos. EP/ 509 K01711X/1, EP/K017144/1, EP/N010345/1, EP/M507799/ 5101, and EP/L016087/1.

References

(1) Akinwande, D., Petrone, N., Hone, J. *Nat. Commun.* **2014**, *5*.

(2) Ryhaenen, T. T., **2010**, Cambridge University Press.

(3) Liu, Z., Chen, G., Liang, B., Yu, G., Huang, H., Chen, D., Shen, G. *Opt. Express* **2013**, *21*, 7799-7810.

(4) Yuan, H.-C., Shin, J., Qin, G., Sun, L., Bhattacharya, P., Lagally, M. G., Celler, G. K., Ma, Z. *Appl. Phys. Lett.* **2009**, *94*, 13102.

(5) Park, S.-I., Xiong, Y., Kim, R.-H., Elvikis, P., Meitl, M., Kim, D.-H., Wu, J., Yoon, J., Yu, C.-J., Liu, Z., et al. *Science* **2009**, *325*, 977-981.

(6) Qiang, Z., Yang, H., Chen, L., Pang, H., Ma, Z., Zhou, W. *App. Phys. Lett.* **2008**, *93*, 061106.

(7) Bosman, E., Van Steenberge, G., Van Hoe, B., Missinne, J., Vanfleteren, J., Van Daele, P. *Photon. Technol. Lett., IEEE* **2010**, *22*, 287-289.

(8) Chen, Z., Ren, W., Gao, L., Liu, B., Pei, S., Cheng, H.-M. *Nat. Mater.* **2011**, *10*, 424-428.

(9) Shahi, S. *Nature Photon.* **2010**, *4*, 506-506.

(10) Yoon, J., Li, L., Semichaevsky, A. V., Ryu, J. H., Johnson, H. T., Nuzzo, R. G., Rogers, J. A. *Nat. Commun.* **2011**, *2*, 343.

(11) Kim, D.-H., Lu, N., Ma, R., Kim, Y.-S., Kim, R.-H., Wang, S., Wu, J., Won, S. M., Tao, H., Islam, A., et al. *Science* **2011**, *333*, 838-843.

(12) Ko, H. C., Stoykovich, M. P., Song, J., Malyarchuk, V., Choi, W. M., Yu, C.-J., Geddes Iii, J. B., Xiao, J., Wang, S., Huang, Y., et al. *Nature* **2008**, *454*, 748-753.

(13) Blakemore, J. S. *J. Appl. Phys.* **1982**, *53*, 123-181.

(14) MacMillan, N. H. *J Mater. Sci.* **1972**, *7*, 239-254.

(15) Yang, W., Yang, H., Qin, G., Ma, Z., Berggren, J., Hammar, M., Soref, R., Zhou, W. *Appl. Phys. Lett.* **2010**, *96*, 121107.

(16) Chen, G., Liang, B., Liu, Z., Yu, G., Xie, X., Luo, T., Xie, Z., Chen, D., Zhu, M.-Q., Shen, G. *J. Mater. Chem. C* **2014**, *2*, 1270-1277.

(17) Lee, S., Jung, S. W., Park, S., Ahn, J., Hong, S. J., Yoo, H. J., Lee, M. H., Cho, D. I. *Proc. IEEE Micr. Elect.*, **2012**.

(18) Yu, G., Liu, Z., Xie, X., Ouyang, X., Shen, G. *J. Mater. Chem. C* **2014**, *2*, 6104-6110.

(19) Sze, S. M., Kwok, K. N. **2006**, Wiley, New York.

(20) Bonaccorso, F., Sun, Z., Hasan, T., Ferrari, A. C. *Nature Photon.* **2010**, *4*, 611-622.

(21) Ferrari, A. C., Bonaccorso, F., Fal'ko, V., Novoselov, K. S., Roche, S., Boggild, P., Borini, S., Koppens, F. H. L., Palermo, V., Pugno, N., et al. *Nanoscale* **2015**, *7*, 4598-4810.

(22) Koppens, F. H. L., Mueller, T., Avouris, P., Ferrari, A. C., Vitiello, M. S., Polini, M. *Nat. Nanotechnol.* **2014**, *9*, 780-793.

(23) Sun, Z. P., Hasan, T., Torrisi, F., Popa, D., Privitera, G., Wang, F. Q., Bonaccorso, F., Basko, D. M., Ferrari, A. C. *Acs Nano* **2010**, *4*, 803-810.

(24) Kim, K. S., Zhao, Y., Jang, H., Lee, S. Y., Kim, J. M., Kim, K. S., Ahn, J.-H., Kim, P., Choi, J.-Y., Hong, B. H. *Nature* **2009**, *457*, 706-710.

(25) Baugher, B. W. H., Churchill, H. O. H., Yang, Y., Jarillo-Herrero, P. *Nat. Nanotechnol.* **2014**, *9*, 262-267.

(26) Pospischil, A., Furchi, M. M., Mueller, T. *Nat. Nanotechnol.* **2014**, *9*, 257-261.

(27) Lopez-Sanchez, O.; Lembke, D.; Kayci, M.; Radenovic, A.; Kis, A. *Nat. Nanotechnol.* **2013**, *8*,497âĂŞ501.

(28) Xia, F.; Mueller, T.; Lin, Y. M.; Valdes-Garcia, A.; Avouris, P. *Nat. Nanotechnol.* **2009**, *4*, 839-843.

(29) Mueller, T., Xia, F. N. A., Avouris, P. *Nat. Photonics* **2010**, *4*, 297-301.

(30) Liu, M., Yin, X. B., Ulin-Avila, E., Geng, B. S., Zentgraf, T., Ju, L., Wang, F., Zhang, X. *Nature* **2011**, *474*, 64-67.

(31) Chen, J., Badioli, M., Alonso-Gonzalez, P., Thongrattanasiri, S., Huth, F., Osmond, J., Spasenovic, M., Centeno, A., Pesquera, A., Godignon, P., et al. *Nature* **2012**, *487*, 77-81.

(32) Echtermeyer, T. J., Britnell, L., Jasnos, P. K., Lombardo, A., Gorbachev, R. V., Grigorenko, A. N., Geim, A. K., Ferrari, A. C., Novoselov, K. S. *Nat. Commun.* **2011**, *2*, 458.

(33) Fei, Z., Rodin, A. S., Andreev, G. O., Bao, W., McLeod, A. S., Wagner, M., Zhang, L. M., Zhao, Z., Thiemens, M., Dominguez, G., et al. *Nature* **2012**, *487*, 82-85.

(34) Ju, L., Geng, B., Horng, J., Girit, C., Martin, M., Hao, Z., Bechtel, H. A., Liang, X., Zettl, A., Shen, Y. R., et al. *Nat. Nanotechnol.* **2011**, *6*, 630-634.

(35) Yan, H., Li, X., Chandra, B., Tulevski, G., Wu, Y., Freitag, M., Zhu, W., Avouris, P., Xia, F. *Nat. Nanotechnol.* **2012**, *7*, 330-334.

(36) Furchi, M. M., Pospischil, A., Libisch, F., BurgdÃűrfer, J., Mueller, T. *Nano Lett.* **2014**, *14*, 4785-4791.

(37) Withers, F., Del Pozo-Zamudio, O., Mishchenko, A., Rooney, A. P., Gholinia, A., Watanabe, K., Taniguchi, T., Haigh, S. J., Geim, A. K., Tartakovskii, A. I., et al. *Nat. Mater.* **2015**, *14*, 301-306.

(38) Hu, P. A., Wang, L. F., Yoon, M., Zhang, J., Feng, W., Wang, X. N., Wen, Z. Z., Idrobo, J. C., Miyamoto, Y., Geohegan, et al. *Nano Lett.* **2013**, *13*, 1649-1654.

(39) Hsiao, Y.-J., Fang, T.-H., Ji, L.-W., Yang, B.-Y. *Nanoscale Res. Lett.* **2015**, *10*, 1-5.

(40) Britnell, L., Ribeiro, R. M., Eckmann, A., Jalil, R., Belle, B. D., Mishchenko, A., Kim, Y. J., Gorbachev, R. V., Georgiou, T., Morozov, S. V., et al. *Science* **2013**, *340*, 1311-1314.

(41) Tamalampudi, S. R., Lu, Y. Y., Kumar, U. R., Sankar, R., Liao, C. D., Moorthy, B. K., Cheng, C. H., Chou, F. C., Chen, Y. T. *Nano Letters* **2014**, *14*, 2800-2806.

(42) Amani, M., Burke, R. A., Proie, R. M., Dubey, M. *Nanotechnology* **2015**, *26*, 115202.

(43) Xue, Y., Zhang, Y., Liu, Y., Liu, H., Song, J., Sophia, J., Liu, J., Xu, Z., Xu, Q., Wang, Z., et al. *Acs Nano* **2016**, *10*, 573-580.

(44) Finn, D. J., Lotya, M., Cunningham, G., Smith, R. J., McCloskey, D., Donegan, J. F., Coleman, J. N. *J. Mater. Chem. C* **2014**, *2*, 925-932.

(45) Withers, F., Yang, H., Britnell, L., Rooney, A. P., Lewis, E., Felten, A., Woods, C. R., Romaguera, V. S., Georgiou, T., Eckmann, A., et al. *Nano Lett.* **2014**, *14*, 3987-3992.

(46) Liu, N., Tian, H., Schwartz, G., Tok, J. B. H., Ren, T.-L., Bao, Z. *Nano Letters* **2014**, *14*, 3702-3708.

(47) Velusamy, D. B., Kim, R. H., Cha, S., Huh, J., Khazaeinezhad, R., Kassani, S. H., Song, G., Cho, S. M., Cho, S. H., Hwang, I., et al. *Nat. Commun.* **2015**, *6*.

(48) Zhang, W. J., Chuu, C. P., Huang, J. K., Chen, C. H., Tsai, M. L., Chang, Y. H., Liang, C. T., Chen, Y. Z., Chueh, Y. L., He, J. H., et al. *Sci. Rep.* **2014**, *4*.

(49) Faraj, M. G., Ibrahim, K., Ali, M. K. M. *Optoelectron. Adv. Mat.* **2011**, *5*, 879-882.

(50) Martins, L. G. P., Song, Y., Zeng, T. Y., Dresselhaus, M. S., Kong, J., Araujo, P. T. *Proc. Natl Acad. Sci. USA* **2013**, *110*, 17762-17767.

(51) Bae, S., Kim, H., Lee, Y., Xu, X., Park, J. S., Zheng, Y., Balakrishnan, J., Lei, T., Kim, H. R., Song, Y. I., et al. *Nat. Nanotechnol.* **2010**, *5*, 574-8.

(52) Thiele, C. and Das, R., Carbon Nanotubes and Graphene for Electronics Applications 2010-2020 **2010**, 98.

(53) Das, A., Pisana, S., Chakraborty, B., Piscanec, S., Saha, S. K., Waghmare, U. V., Novoselov, K. S., Krishnamurthy, H. R., Geim, A. K., Ferrari, A. C., Sood, A. K. *Nat. Nanotechnol.* **2008**, *3*, 210-5.

(54) Das, A., Chakraborty, B., Piscanec, S., Pisana, S., Sood, A. K., Ferrari, A. C. *Phys. Rev. B* **2009**, *79*, 155417.

(55) Choi, M. S., Lee, G. H., Yu, Y. J., Lee, D. Y., Lee, S. H., Kim, P., Hone, J., Yoo, W. J., *Nat. Commun.* **2013**, *4*, 1624.

(56) Das, S., Chen, H. Y., Penumatcha, A. V., Appenzeller, J., *Nano Lett.* **2013**, *13*, 100-105.

(57) Shan, B., Cho, K. *Phys. Rev. Lett.* **2005**, *94*, 236602.

(58) Yu, Y.-J., Zhao, Y., Ryu, S., Brus, L. E., Kim, K. S., Kim, P. *Nano Lett.* **2009**, *9*, 3430-3434.

(59) Kim, B. J., Jang, H., Lee, S.-K., Hong, B. H., Ahn, J.-H., Cho, J. H. *Nano Lett.* **2010**, *10*, 3464-3466.

(60) Lee, S. K., Jang, H. Y., Jang, S., Choi, E., Hong, B. H., Lee, J., Park, S., Ahn, J. H. *Nano Lett.* **2012**, *12*, 3472-3476.

(61) Dumcenco, D., Ovchinnikov, D., Marinov, K., Lazic, P., Gibertini, M., Marzari, N., Sanchez, O. L., Kung, Y.-C., Krasnozhon, D., Chen, M.-W. et al. *Acs Nano* **2015**, *9*, 4611-4620.

(62) Li, X. S., Cai, W. W., An, J. H., Kim, S., Nah, J., Yang, D. X., Piner, R., Velamakanni, A., Jung, I., Tutuc, E., et al. *Science* **2009**, *324*, 1312-1314.

(63) Verble, J. L., Wieting, T. J. *Phys. Rev. Lett.* **1970**, *25*, 362-365.

(64) Wieting, T. J., Verble, J. L. *Phys. Rev. B* **1971**, *3*, 4286-4292.

(65) Lee, C., Yan, H. G., Brus, L. E., Heinz, T. F., Hone, J., Ryu, S. *Acs Nano* **2010**, *4*, 2695-2700.

(66) Li, H., Zhang, Q., Yap, C. C. R., Tay, B. K., Edwin, T. H. T., Olivier, A., Baillargeat, D. *Adv. Funct. Mater.* **2012**, *22*, 1385-1390.

(67) Porto, S. P. S., Krishnan, R. S. *J. Chem. Phys.* **1967**, *47*, 1009-1012.

(68) Lagatsky, A. A., Sun, Z., Kulmala, T. S., Sundaram, R. S., Milana, S., Torrisi, F., Antipov, O. L., Lee, Y., Ahn, J. H., Brown, C. T. A., et al. *Appl. Phys. Lett.* **2013**, *102*, 013113.

(69) Ferrari, A. C., Basko, D. M. *Nat. Nanotechnol.* **2013**, *8*, 235-46.

(70) Ferrari, A. C., Meyer, J. C., Scardaci, V., Casiraghi, C., Lazzeri, M., Mauri, F., Piscanec, S., Jiang, D., Novoselov, K. S., Roth, S., et al. *Phys. Rev. Lett.* **2006**, *97*, 187401.

(71) Cancado, L. G., Jorio, A., Ferreira, E. H., Stavale, F., Achete, C. A., Capaz, R. B., Moutinho, M. V., Lombardo, A., Kulmala, T. S., Ferrari, A. C. *Nano Lett.* **2011**, *11*, 3190-6.

(72) Ferrari, A. C., Robertson, J. *Phys. Rev. B* **2000**, *61*, 14095-14107.

(73) Basko, D. M., Piscanec, S., Ferrari, A. C. *Phys. Rev. B* **2009**, *80*, 165413.

(74) Bruna, M., Ott, A. K., Ijas, M., Yoon, D., Sassi, U., Ferrari, A. C. *Acs Nano* **2014**, *8*, 7432-7441.

(75) Mak, K. F., Lee, C., Hone, J., Shan, J., Heinz, T. F. *Phys. Rev. Lett.* **2010**, *105*, 136805.

(76) Bonaccorso, F., Lombardo, A., Hasan, T., Sun, Z. P., Colombo, L., Ferrari, A. C. *Mater. Today* **2012**, *15*, 564-589.

(77) Boerio, F. J., Bahl, S. K., McGraw, G. E. *J. Poly. Sci.* **1976**, *14*, 1029-1046.

(78) Qiu, D. Y., da Jornada, F. H., Louie, S. G. *Phys. Rev. Lett.* **2013**, *111*, 216805.

(79) Nair, R. R., Blake, P., Grigorenko, A. N., Novoselov, K. S., Booth, T. J., Stauber, T., Peres, N. M. R., Geim, A. K. *Science* **2008**, *320*, 1308-1308.

(80) Novoselov, K. S., Geim, A. K., Morozov, S. V., Jiang, D., Katsnelson, M. I., Grigorieva, I. V., Dubonos, S. V., Firsov, A. A. *Nature* **2005**, *438*, 197-200.

(81) Lemme, M. C., Echtermeyer, T. J., Baus, M., Kurz, H. *IEEE Electr. Device L.* **2007**, *28*, 282-284.

(82) Wehling, T. O., Novoselov, K. S., Morozov, S. V., Vdovin, E. E., Katsnelson, M. I., Geim, A. K., Lichtenstein, A. I. *Nano Lett.* **2008**, *8*, 173-177.

(83) Ye, J. T., Craciun, M. F., Koshino, M., Russo, S., Inoue, S., Yuan, H. T., Shimotani, H., Morpurgo, A. F., Iwasa, Y. *Proc. Natl Acad. Sci. USA* **2011**, *108*, 13002-13006.

(84) Sirringhaus, H., Kawase, T., Friend, R. H., Shimoda, T., Inbasekaran, M., Wu, W., Woo, E. P. *Science* **2000**, *290*, 2123-2126.

(85) Azais, P., Duclaux, L., Florian, P., Massiot, D., Lillo-Rodenas, M.-A., Linares-Solano, A., Peres, J.-P., Jehoulet, C., BÃl'guin, F. *J. Power Sources* **2007**, *171*, 1046-1053.

(86) Efetov, D. K., Kim, P. *Phys. Rev. Lett.* **2010**, *105*, 256805.

(87) Konstantatos, G., Badioli, M., Gaudreau, L., Osmond, J., Bernechea, M., de Arquer, G., Gatti, F., Koppens, F. H. L. *Nat. Nanotechnol.* **2012**, *7*, 363-368.

(88) Meric, I., Han, M. Y., Young, A. F., Ozyilmaz, B., Kim, P., Shepard, K. L. *Nat. Nanotechnol.* **2008**, *3*, 654-659.

(89) Robinson, J. A., LaBella, M., Zhu, M., Hollander, M., Kasarda, R., Hughes, Z., Trumbull, K., Cavalero, R., Snyder, D. *Appl. Phys. Lett.* **2011**, *98*, 053103.

(90) Xia, J., Chen, F., Li, J., Tao, N. *Nat. Nanotechnol.* **2009**, *4*, 505-509.

(91) Fang, T., Konar, A., Xing, H., Jena, D. *Appl. Phys. Lett.* **2007**, *9*, 092109.

(92) Ozel, T., Gaur, A., Rogers, J. A., Shim, M. *Nano Lett.* **2005**, *5*, 905-911.

(93) Lu, C., Fu, Q., Huang, S., Liu, J. *Nano Lett.* **2004**, *4*, 623-627.

(94) Russel, W.B., Saville, D.A. and Schowalter, W. R. **1989**, Cambridge University Press, UK.

(95) Salomon, M., Xu, M., Eyring, E. M., Petrucci, S. *J. Phys. Chem.* **1994**, *98*, 8234âĂŞ8244.

(96) Boyd, R. H. *J. Polym. Sci. Polym. Phys.* **1983**, *21*, 505âĂŞ514.

(97) Zhang, Y. B., Tan, Y. W., Stormer, H. L., Kim, P. *Nature* **2005**, *438*, 201-204.

(98) Adam, S., Hwang, E. H., Galitski, V. M., Sarma, S. D. *Proc. Natl. Acad. Sci. USA* **2007**, *104*, 18392-18397.

(99) Chen, J. H., Jang, C., Adam, S., Fuhrer, M. S., Williams, E. D., Ishigami, M. *Nature Phys.* **2008**, *4*, 377-381.

(100) Victor, M. G., Shaffique, A., Sarma, S. D. *Phys. Rev. B* **2007**, *76*, 245405.